Conformation and Dynamics of Atactic Poly(acrylonitrile). 2. Torsion Angle Distributions in Meso Dyads from Two-Dimensional Solid-State Double-Quantum ^{13}C NMR

Hironori Kaji*,†,‡ and Klaus Schmidt-Rohr‡,§

Department of Polymer Science and Engineering, University of Massachusetts, Amherst, Massachusetts 01003, Institute for Chemical Research, Kyoto University, Uji, Kyoto 611-0011, Japan, and Department of Chemistry and Ames Laboratory, Iowa State University, Ames, Iowa 50011

Received April 16, 2001; Revised Manuscript Received July 5, 2001

ABSTRACT: The average trans torsion angles and their distributions have been investigated for meso dyads in a disordered crystalline polymer, atactic poly(acrylonitrile) (aPAN), by two-dimensional (2D) solid-state ^{13}C double-quantum NMR spectroscopy (DOQSY). The 2D DOQSY spectra of an aPAN sample with ^{13}C-labeled nitrile side groups show significant deviations from the ideal trans conformations. The $^{13}C{\equiv}N$ bonds in meso trans−trans dyads make an average angle of 20° with each other, with distributions of 25° standard deviation. This translates into standard deviations of $\sigma = 20°$ for the two successive torsion angles in these dyads. The experimental spectrum constrains the average torsion angles to a line between ($+160 \pm 10°$, $+160 \pm 10°$) and ($\pm 170 \pm 5°$, $\mp 170 \pm 5°$), with distributions of standard deviation $\sigma = 20 \pm 5°$ for both torsion angles. It is also confirmed that the trans:gauche ratio of backbone bonds in aPAN is 90:10 (±5%). The high trans content is apparently enabled by the torsion angle deviations from the ideal trans state in meso trans−trans dyads, which alleviate the steric hindrance and the large electric dipole interaction between the CN groups and thus lower the intramolecular conformational energy.

1. Introduction

The quantitative description of the local structure in disordered polymers is one of the long-standing problems in polymer science. For glassy polymers, the chain conformation has been theoretically predicted from unperturbed random conformational statistics, using the rotational isomeric state (RIS) model.[1,2] Predictions of the RIS model were recently confirmed experimentally in glassy polymers by two-dimensional (2D) double-quantum (DQ) solid-state nuclear magnetic resonance (NMR) spectroscopy[3,4] (DOQSY).[5] The conformation of disordered crystalline polymers is more difficult to access theoretically because not only intramolecular but also intermolecular interactions will affect the local conformation. Therefore, in the crystalline state the polymer does not necessarily take the lowest-energy conformation of the isolated chain.[3]

In a preceding paper,[6] we investigated the backbone conformation in a partially disordered polymer, atactic poly(acrylonitrile) (aPAN), by measuring relative CH_2 group orientations on a 15% $^{13}CH_2$-carbon-labeled aPAN ($^{13}CH_2$-aPAN) sample, using DOQSY techniques. The backbone conformation in aPAN was successfully determined as trans:gauche = 90%:10% (±10%) by these experiments. However, torsion angles in the trans and gauche states are still ambiguous because the chemical shift tensor orientation of CH_2 carbons is not sufficiently well-defined. Furthermore, torsion angles in trans states of meso dyads and racemo dyads are expected to be different because of the steric hindrance and electronic dipole repulsive force of $-C{\equiv}N$ groups in meso dyads.[7−9] Recently, Robyr et al.[10] estimated the conformation of meso and racemo dyads separately for atactic polystyrene (aPS), extracting the information for meso dyads from isotactic PS (iPS). However, conformations of meso dyads in atactic polymers are not necessarily the same as those in isotactic polymers; therefore, it is preferable to determine the conformation of meso dyads directly from an atactic sample.

In this paper, we quantitatively characterize the conformations of meso dyads directly in an aPAN sample. For this purpose, the 2D DOQSY technique is applied to 100% $^{13}C{\equiv}N$-carbon-labeled aPAN (^{13}CN-aPAN) (Figure 1). In contrast to the DOQSY experiment of $^{13}CH_2$-aPAN presented in the preceding paper,[6] there is no ambiguity in the chemical shift tensor orientation of $^{13}C{\equiv}N$ carbons, since the axially symmetric chemical shift anisotropy (CSA) of the $^{13}C{\equiv}N$ carbons probes specifically the $C{\equiv}N$ triple-bond directions. A much better angular resolution than in the previous $^{13}CH_2$ experiments is obtained due to the much larger CSA width of the $^{13}C{\equiv}N$ carbons. Moreover, the meso trans−trans (*mTT*) and racemo trans−trans (*rTT*) dyads give very different DOQSY powder patterns, due to the different relative orientations of adjacent $^{13}C{\equiv}N$ groups. More specifically, the successive $C{\equiv}N$ groups in *mTT* dyads are more or less parallel, while those in *rTT* dyads make an angle of ca. 120° with each other. The spectrum of the *mTT* dyads is concentrated near the slope-two diagonal, and the distance between adjacent $C{\equiv}N$ groups in *mTT* dyads is mostly shorter than in racemo dyads, resulting in a more efficient excitation of the DQ coherence in *mTT* dyads. Therefore, the average torsion angles and their distributions can be determined quite selectively for *mTT* dyads by this experiment.

2. Experimental Section

2.1. Samples. A powdered 100% 1-^{13}C-labeled aPAN (^{13}CN-aPAN) sample was polymerized from [1-^{13}C]acrylonitrile. The

* To whom correspondence should be addressed at Kyoto University. E-mail: kaji@molmat.kuicr.kyoto-u.ac.jp.
† Kyoto University.
‡ University of Massachusetts.
§ Iowa State University.

10.1021/ma010657k CCC: $20.00
Published on Web 09/13/2001

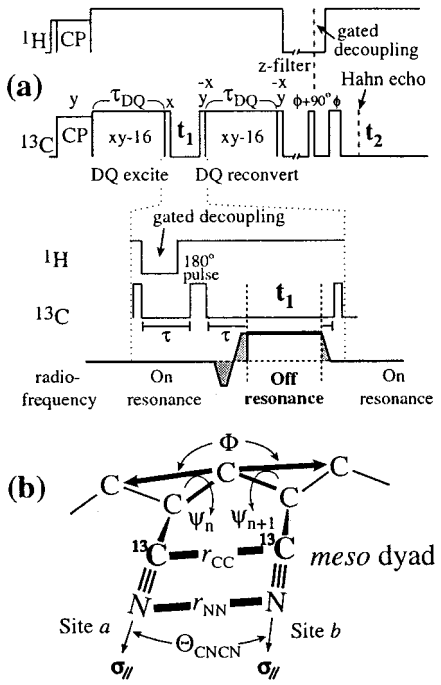

Figure 1. (a) Pulse sequence of the solid-state ^{13}C 2D DOQSY experiment[5] with an *xy*-16 180° pulse train[16,17] to refocus the ^{13}C chemical shift constantly and thus keep the ^{13}C homonuclear dipolar interaction in the strong coupling limit. CP = cross-polarization from ^{1}H to ^{13}C. The frequency switch indicated at the bottom of the figure is explained in the Appendix. Periods of gated decoupling for dipolar dephasing of the double-quantum and the single-quantum coherences involving C−H sites are indicated. The 180° pulses before t_1 evolution and before detection generate Hahn echoes to avoid dead-time effects. (b) Geometry of a meso dyad of PAN, with torsion-angle-dependent internuclear distances (r_{CC} and r_{NN}) and intersegmental angles (Θ_{CNCN}, and Φ between local chain axes) indicated.

details of the polymerization procedure, processing, and characterization of the polymerized sample were described in our preceding paper.[6] The viscosity average molecular weight was 1.2×10^5, and the triad tacticity measured by solution ^{13}C NMR was *mm*:*mr*:*rr* = 29:50:21. The wide-angle X-ray diffraction (WAXD) pattern showed the pseudohexagonal chain packing, which is the most commonly reported polymorph.[7,11−14]

2.2. NMR Measurements. The solid-state NMR experiments were performed on a Bruker DSX-300 spectrometer in a static magnetic field of 7 T. The isotropic ^{13}CN-aPAN powder sample was inserted as a cylindrical block into a 4.5 mm diameter coil of a stationary Bruker ^{1}H−^{13}C double-resonance probe. The measurement was carried out at 298 K without sample rotation. Cosine data sets were measured off-resonance in ω_1 and processed to yield purely absorptive, nonquadrature spectra. Since the phase structure of aPAN is not well understood yet,[15] we measured all the components in aPAN, without using any filters for the selection of certain morphological components. A detailed discussion of the phase structure of aPAN is given in ref 6. The pulse sequence for 2D ^{13}C homonuclear DOQSY NMR experiments to be applied to ^{13}CN-aPAN is shown in Figure 1. The ^{1}H and ^{13}C 90° pulse lengths were 2.3 and 2.1 μs, respectively. A cross-polarization time of 2 ms, a recycle delay of 8 s, a *z*-filter before detection of 2 ms, an acquisition time of 3.12 ms, a dwell time of 6 μs, and ^{1}H decoupling fields $\gamma\mathbf{B}_1/2\pi$ of 88 kHz were used. The DQ excitation and reconversion delays, τ_{DQ} = 0.8 ms, each contained two cycles of the *xy*-16 pulse sequence[16,17] with windows of τ' = 20.8 μs. The ^{13}C frequency was switched 30 kHz off-resonance during the t_1 evolution time; each switching time was 8 μs. The theoretical background of the ^{13}C frequency switches is described in the Appendix. The pulses were applied at a frequency near the center of the powder spectrum. The τ delay for the Hahn echo was 25 μs. During the Hahn echo, ^{1}H decoupling was turned off for 22 μs to dephase the signal of natural-abundance aliphatic ^{13}C. Some residual aliphatic ^{13}C signals are observed in the obtained 2D DOQSY spectrum, but longer dephasing times would reduce the ^{13}CN signals. In the t_1 dimension, 100 slices with increments of 3 μs were acquired, with 128 scans per t_1 slice. The total acquisition time was 28.4 h.

3. NMR Background

3.1. Angle-Dependent NMR Frequencies. The NMR frequency reflects the orientation of a given molecular unit relative to the external magnetic field $\mathbf{B}_0$. For carbons in $-^{13}$C≡N groups, the chemical shift tensor is uniaxial and the unique principal axis (labeled $\sigma_{\parallel}$) is directed along the $-^{13}$C≡N bonds, as shown in Figure 1b. The NMR frequency is then described as[18]

$$\omega_{aniso}(\theta) = \frac{\delta_{aniso}}{2}(3\cos^2\theta - 1) \qquad (1)$$

where θ is the angle between the $-^{13}$C≡N and $\mathbf{B}_0$ directions. In the following, the orientation-dependent frequencies, ω_{aniso}, appear as ω_a or ω_b for $-^{13}$C≡N carbons.

3.2. 2D DOQSY Experiment. The 2D DOQSY pulse sequence for a ^{13}CN-aPAN sample, shown in Figure 1a, is similar to the DOQSY pulse sequence in the preceding papers[3−6,19,20] but modified for the present measurements. The modifications are as follows. During the DQ excitation and reconversion periods, the *xy*-16 sequence of π pulses is applied with phases of $x\ y\ x\ y\ y\ x\ y\ x\ -x\ -y\ -x\ -y\ -y\ -x\ -y\ -x$.[16,17] This sequence continues to refocus the chemical shift during the DQ excitation and reconversion periods, so that all the spin pairs are in the strong coupling limit. This simplifies the analysis of the 2D DOQSY spectra. Another advantage of this sequence is that we can obtain a 1.5-fold intensity increase theoretically at short excitation times ($\nu_D\tau_{DQ} \ll 1$). In the actual experiments, a ∼1.7-fold intensity increase was observed at τ_{DQ} = 0.8 ms. Note that τ_{DQ} in this paper corresponds to 2τ in our preceding papers.[3−5,19,20] Gated decoupling is applied before the t_1 evolution and t_2 detection periods. This dephases undesirable signals of aliphatic CH_2 and CH groups containing ^{13}C in natural abundance. A frequency-switch technique is applied, which yields artifact-free DOQSY spectra even for nuclei with large CSA widths. A version with three switching times and a Hahn echo (see the Appendix) gives us time for gated decoupling before t_1 evolution. A simple 180° pulse is applied to generate a Hahn echo before detection, and detection is carried out without ^{13}C−^{13}C homonuclear dipolar decoupling. The strongest ^{13}C−^{13}C dipolar coupling between the labeled ^{13}CN carbons with the nearest distance, 2.52 Å, in the strong coupling limit, ν_D = 0.7 kHz, is much smaller than the CSA width of the ^{13}C≡N carbon of aPAN, 363 ppm (27.4 kHz at 7 T). Thus, a simple Hahn echo and detection without ^{13}C−^{13}C dipolar decoupling are sufficient for the present sample. The pulse sequence can be described as follows, focusing only on the relevant terms in the density operator:

$$\text{DQ excitation: } S_y + L_y \xrightarrow{H_D(xy\text{-}16)\tau_{DQ}} -2(S_xL_z + L_xS_z)\sin\left(\frac{3}{2}\omega_D\tau_{DQ}\right)$$

$$\xrightarrow{(\pi/2)(S_x + L_x)} -2(S_xL_y + L_xS_y)\sin\left(\frac{3}{2}\omega_D\tau_{DQ}\right)$$

$$\text{DQ evolution in } t_1\text{: } \xrightarrow{(\omega_a S_z + \omega_b L_z)t_1} -2(S_xL_y + L_xS_y)\sin\left(\frac{3}{2}\omega_D\tau_{DQ}\right)\cos[(\omega_a + \omega_b)t_1] \quad (2)$$

$$\text{DQ reconversion: } \xrightarrow{(\pi/2)(S_{-x} + L_{-x})} -2(S_xL_z + L_xS_z)\sin\left(\frac{3}{2}\omega_D\tau_{DQ}\right)\cos[(\omega_a + \omega_b)t_1]$$

$$\xrightarrow{H_D(xy\text{-}16)\tau_{DQ}} -2(S_y + L_y)\sin^2\left(\frac{3}{2}\omega_D\tau_{DQ}\right)\cos[(\omega_a + \omega_b)t_1]$$

where $H_D(xy\text{-}16)$ is the homonuclear dipolar Hamiltonian in the strong coupling limit. Cosine components in the DQ excitation and reconversion periods, which give zero-frequency artifacts, are subtracted by standard DQ phase cycling. According to eq 2, the final result is a modulation of the ^{13}C signal in the detection period t_2. The 2D time domain signal is thus

$$S(t_1,t_2) = g_{SCL}{}^2(\tau_{DQ})[\cos[(\omega_a + \omega_b)t_1]][\exp(i\omega_a t_2) + \exp(i\omega_b t_2)] \quad (3)$$

where

$$g_{SCL}(\tau_{DQ}) = \sin\left(\frac{3}{2}\omega_D\tau_{DQ}\right) \quad (4)$$

Thus, the ^{13}C homonuclear correlation spectrum with the sum of orientation-dependent frequencies, $\omega_a + \omega_b$, in the t_1 dimension and the individual frequencies, ω_a or ω_b, in the t_2 dimension can be obtained. The intensity is weighted by the factor $g_{SCL}{}^2(\tau_{DQ})$, which depends on the dipolar coupling between the two carbons.

3.3. Geometry of aPAN Chain and Designation of Torsion Angles. On the basis of the geometry of a PAN meso dyad as shown in Figure 1b, parts a and b of Figure 2 indicate the torsion angle dependence of the C−C and N−N distances in two successive $^{13}C{\equiv}N$ groups in meso dyads. The contour lines are labeled in Ångströms. The dotted region indicates distances shorter than 2.52 Å, the C−C distance in the exact (180°, 180°) *TT* conformation. In the following simulation, conformations whose C−C distance or N−N distance is shorter than 2.52 Å are excluded. Although the shortest N−N distance is shorter than the shortest C−C distance, the dotted area of Figure 2b lies fully within that of Figure 2a. Therefore, it is sufficient to consider the C−C distance to avoid steric interference of two CN groups.

The designation of the torsion angle used in this paper is the same as that in our preceding paper:[6] Conformations with torsion angles within ±30° from ±180°, ±120°, ±60°, and ±0° are designated as trans (*T*), anticlinal (*A*), gauche (*G*), and cis (*C*), respectively. In this paper, distributions of torsion angles are introduced, and as a result a peak in the torsion angle distribution may extend beyond a single region. In our nomenclature, the designations of *T*, *G*, etc. are used for the "average" torsion angle, i.e., the center of a given peak in the torsion angle distribution. For the two different gauche conformations, we use the definition of *G* and $\bar{G}$, which are assigned torsion angles within ±30° from +60° and −60°, respectively. These are discussed in detail in our preceding paper.[6]

Figure 2c shows the torsion angle dependence of the angle Θ_{CNCN} between the C≡N bonds in two successive $^{13}C{\equiv}N$ groups in meso dyads. The values of 0° and 180° correspond to parallel and antiparallel alignments, respectively. The CN−CN electric dipolar interactions, which are expected to induce disorder of chain conformations, are a function of the CN−CN angles and distances. The 2D DOQSY spectra shown below are mainly determined by Θ_{CNCN}, and modulated by $^{13}C{-}^{13}C$ distances and angles of the $^{13}C{-}^{13}C$ internuclear vector relative to the external magnetic field, $\mathbf{B}_0$.

Figure 2d displays the torsion angle dependence of the angle between the local chain axes on both sides of the relevant two torsion angles. The value of 180° corresponds to straight zigzag chains. Smaller local-chain-axis angles make it difficult to form laterally ordered crystals of aPAN. In the calculations, the bond length for backbone C−C is 1.54 Å; for side group C−C 1.46 Å; and for C≡N 1.16 Å. The bond angle for backbone $\angle C^{\alpha}{-}C{-}C^{\alpha}$ is 109.5°, and for side groups $\angle C{-}C^{\alpha}{-}CN = 109.5°$.

3.4. ^{13}C Labeling and Intermolecular Correlation. Due to the large CSA width of 363 ppm, 100% isotopic labeling of the ^{13}CN carbon site of aPAN is necessary to obtain a reasonable signal-to-noise ratio. The undesirable DQ coherences that involve three or more spins are known to give negative signals,[21] and they are relatively small.[4] Since the three-spin signals are observed not only in the lozenge-shaped region accessible to the desired two-spin DQ spectrum but also outside this region in a larger square, we can estimate the contribution from negative signals outside the two-spin lozenge. The volume intensity of negative signals in that region of the experimental 2D DOQSY spectrum (shown below) was less than 1% of the total. Therefore, the effect of DQ coherences of three or more spins can apparently be neglected.

In contrast, the overlap with interchain DQ coherences is inevitable, because all the chains are 100% ^{13}C-labeled. In contrast to the 15% $^{13}CH_2$-labeled aPAN in our previous work, the intramolecular distances of the four-bond-separated $^{13}CN{-}^{13}CN$ carbons are widely distributed depending on the conformation and tacticity. Roughly speaking, the distances are 2.5−3.5, ∼4, and ∼3.5 Å for *mTT*, meso trans−gauche (*mTG*), and *rTT* dyads, respectively (see Figure 2a for meso dyads). While the distance between the centers of neighboring chains is 6 Å, the ^{13}CN carbon is relatively far from the center of the chain, indicating that the $^{13}C{-}^{13}C$ intermolecular distances can be shorter than 6 Å. Therefore, the contribution of intermolecular $^{13}C{-}^{13}C$ correlations should be taken into account to explain the experimental DOQSY spectrum. Since this polymer has lateral order with pseudohexagonal packing as revealed from WAXD patterns,[7,11−14] specific orientational correlations should be considered for the interchain correlation. Details of the interchain correlation are discussed in the following paper in this issue.[22]

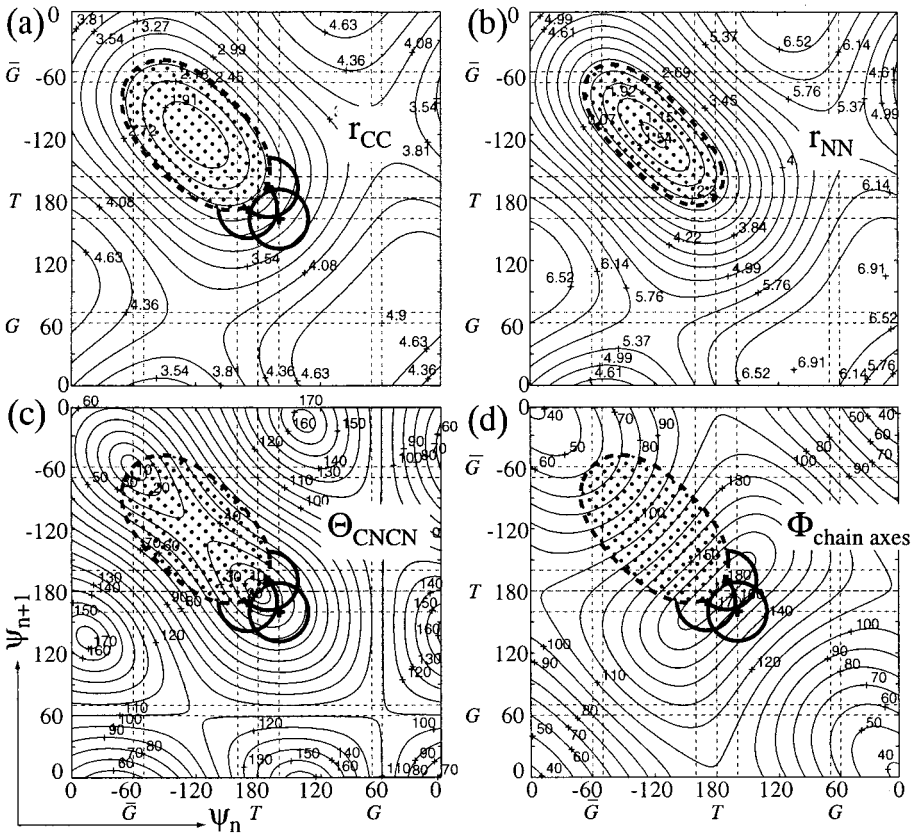

Figure 2. Geometrical maps of aPAN in the meso dyads (see Figure 1b for definitions of distances and angles). (a) Intramolecular four-bond C−C distance r_{CC} of adjacent C≡N side groups (Å). (b) Intramolecular six-bond N−N distance r_{NN} of adjacent C≡N side groups (Å). (c) Angle Θ_{CNCN} between C≡N bonds in adjacent side groups (deg). (d) Angle Φ between local chain axes on both sides of the relevant two backbone bonds (deg). All the maps are plotted as a function of the two torsion angles ψ_n, ψ_{n+1} of the backbone bonds between the relevant C≡N side groups. Conformations with CN−CN distances shorter than 2.52 Å are excluded from the simulations in Figures 5, 7, and 8. The corresponding regions within 2.52 Å are shown dotted in (a), (c), and (d) for C−C distances and in (b) for N−N distances. The thick circles indicate the conformational regions of (+160°, +160°, σ = 20°) and (±170°, ∓170°, σ = 20°) (see the text for the notation), both of which give best-fit simulations of the experimental 2D DOQSY spectrum. The central portions of these plots are shown enlarged in Figure 6.

4. Results and Discussion

4.1. One-Dimensional CSA Experiments. At the top and bottom of Figure 3a, the experimental and simulated ^{13}C CSA powder patterns of ^{13}CN-aPAN are shown, respectively. A three-line splitting of the downfield peak due to the directly bonded ^{13}C≡^{14}N dipolar coupling is observed. The three lines can be considered to correspond to the three ^{14}N quantum states labeled by m = −1, 0, +1. The splitting of 1.283 kHz (17 ppm at 7 T) corresponds to a ^{13}C≡^{14}N distance of 1.19 Å. This agrees well with the typical C≡N distance from X-ray diffraction, electron diffraction, and microwave spectroscopy, 1.16−1.17 Å,[7,23,24] if we take into account that the internuclear distances obtained from solid-state NMR methods are normally 1−4% longer than those obtained from X-ray diffraction.[25]

No segmental motion is considered in the simulations. At room temperature, the C≡N group in aPAN undergoes only small-angle librational motion, whose effect on 1D CSA spectra can be incorporated into the principal values of the CSA. The effect of motion on the 2D spectra is also negligible, since the total duration of DQ reconversion and *z*-filter periods, during which interfering motion might occur, is quite short (less than 3 ms). This is confirmed by 2D CSA exchange experiments for a ^{15}N-labeled aPAN sample, as described in our preceding paper.[6] The CSA is axially symmetric, and a simulated spectrum with principal values of ($\sigma_\perp$, $\sigma_\parallel$) = (243, −120), (226, −86), and (209, −52) ppm with a Gaussian broadening of 4 ppm reproduces the experimental 1D CSA spectrum of ^{13}CN-aPAN, as shown at the bottom of Figure 3a. The resulting isotropic chemical

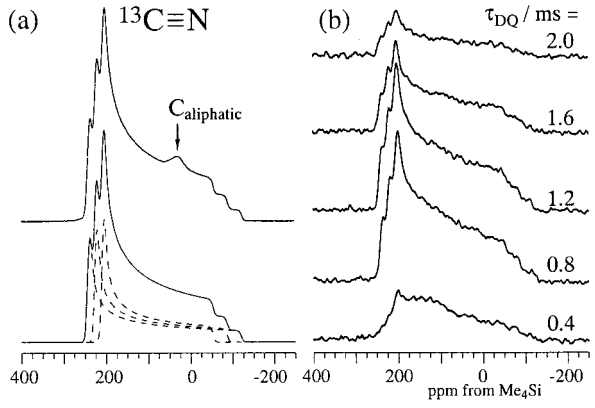

Figure 3. (a) Top: Experimental one-dimensional CSA spectrum of ^{13}CN-aPAN. The small peak at 0−50 ppm is due to aliphatic carbons. Bottom: Corresponding simulated spectrum with the three-component spectra shown by dashed lines. For the simulation, the principal value sets of ($\sigma_\perp$, $\sigma_\parallel$) = (243, −120), (226, −86), and (209, −52) ppm were used, with a Gaussian broadening of 4 ppm standard deviation. (b) Experimental double-quantum filtered spectra (the ω_2 Fourier transform of the t_1 = 1 μs slice of 2D DOQSY data) at different τ_{DQ} times.

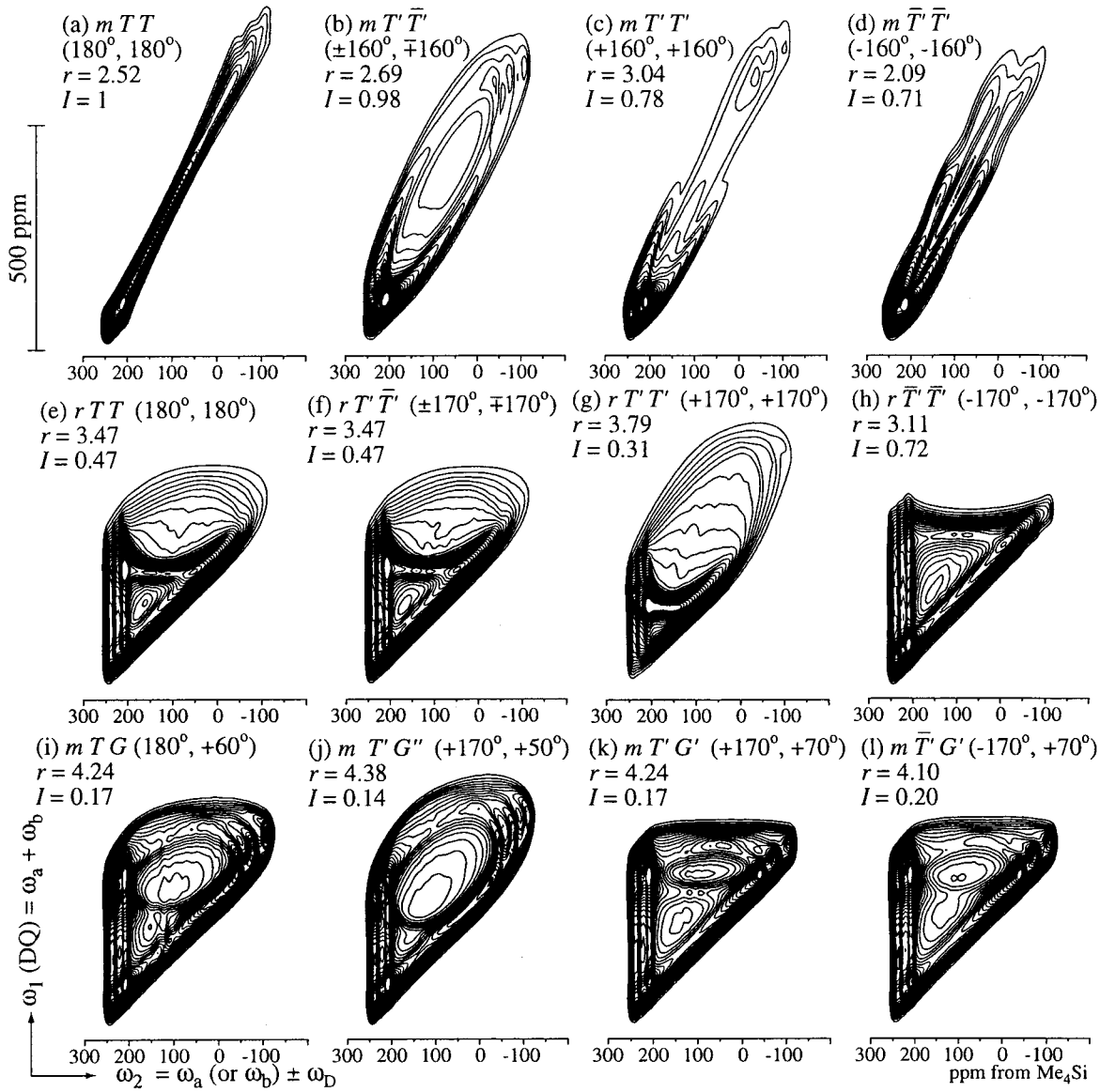

Figure 4. Simulated 2D DOQSY spectra of ^{13}CN-aPAN in the strong coupling limit for typical conformations of *mTT*, *rTT*, and *mTG* in the top, second, and third rows, respectively. The dyad configurations and two successive torsion angle values are indicated above each spectrum. The $^{13}C-^{13}C$ distance, *r*, between the two relevant C≡N carbons and the volume intensities, *I*, of the DQ spectrum relative to the exact *mTT* state are also given. Parameters used for the simulations are as follows: $\angle C^{\alpha}-C-C^{\alpha} = \angle C-C^{\alpha}-CN = 109.5°$, $r(C-C^{\alpha}) = 1.54$ Å, $r(C^{\alpha}-CN) = 1.46$ Å and a DQ excitation time of $\tau_{DQ} = 0.8$ ms. To account for the combined effect of ^{13}C CSA and $^{13}C\equiv^{14}N$ dipolar coupling, nine spectral patterns, with all combinations of the spectral ranges with $\sigma_{\perp}$ of 243, 226, and 209 ppm, and $\sigma_{\parallel}$ of −52, −86, and −120 ppm in both dimensions, were summed up. Gaussian broadenings with standard deviations of 5 and 12.5 ppm were applied along ω_1 and ω_2, respectively. Thirty contour lines are plotted between 3% and 90% of the maximum intensity.

shift, 122 ppm, agrees with the isotropic chemical shift obtained under MAS, 121.8 ppm.

4.2. DQ Excitation Time Dependence of the DQ Intensity and Spectra. Before the 2D NMR experiments, the buildup of the DQ intensity as a function of τ_{DQ} is briefly described. This is a convenient index of the nearest typical distance *r* between the two labeled ^{13}C sites. The DQ signal intensities are determined by the factor $g_{SCL}{}^2(\tau_{DQ})$, as shown in eqs 3 and 4. The $^{13}C-^{13}C$ dipolar coupling, ω_D, is given by

$$\omega_D = \frac{\mu_0}{4\pi}\hbar\frac{\gamma_1\gamma_2}{r^3} = 2\pi(7.5\text{ kHz})\frac{1}{(r/\text{Å})^3} \qquad (5)$$

The factor of 1.5 for the strong coupling limit is considered in eq 4. From eqs 4 and 5, the factor of DQ excitation and reconversion, $g_{SCL}{}^2(\tau_{DQ})$, is calculated as a function of *r* and τ_{DQ}:

$$g_{SCL}{}^2(\tau_{DQ}) = \left\langle \sin^2\left(2\pi(11.25\text{ kHz})\frac{(\tau_{DQ}/\text{ms})}{(r/\text{Å})^3}\right)\right\rangle \qquad (6)$$

The angular brackets indicate the powder average. Figure 3b shows the experimental τ_{DQ} dependence of the first slice of DQ spectra of ^{13}CN-aPAN in the strong coupling limit. The maximum intensity is obtained at ca. 0.8 ms. This suggests that the average closest distance of two ^{13}C nuclei in ^{13}CN groups of aPAN is roughly 3−4 Å.

4.3. 2D DOQSY Experiments. 4.3.1. 2D DOQSY Simulations in the Strong Coupling Limit. Figure 4 shows simulated 2D DOQSY spectra of ^{13}CN-aPAN

Table 1. Quantum States of ^{14}N Directly Bonded to Labeled ^{13}C Carbons[a]

(a) 2D exchange experiment without ^{14}N relaxation

	m in t_2(SQ)		
m in t_1(SQ)	−1	0	+1
+1			+1, +1
0		0,0	
−1	−1, −1		

(b) 2D exchange experiment with ^{14}N relaxation

	m in t_2(SQ)		
m in t_1(SQ)	−1	0	+1
+1	+1, −1	+1, 0	+1, +1
0	0, −1	0, 0	0, +1
−1	−1, −1	−1, 0	−1, +1

(c) 2D DOQSY experiment without ^{14}N relaxation

	m in t_2(SQ)		
m in t_1(DQ)	−1	0	+1
+2			(+1, +1), +1
+1		(0, +1), 0	(+1, 0), +1
0	(−1, +1), −1	(0, 0), 0	(+1, −1), +1
−1	(−1, 0), −1	(0, −1), 0	
−2	(−1, −1), −1		

(d) 2D DOQSY experiment with ^{14}N relaxation

	m in t_2(SQ)		
m in t_1(DQ)	−1	0	+1
+2	(+1, +1) , −1	(+1, +1), 0	(+1, +1), +1
+1	(+1, 0), −1 (0, +1), −1	(+1, 0), 0 (0, +1), 0	(+1, 0), +1 (0, +1), +1
0	(+1, −1), −1 (0, 0), −1 (−1, +1), −1	(+1, −1), 0 (0, 0), 0 (−1, +1), 0	(+1, −1), +1 (0, 0), +1 (−1, +1), +1
−1	(0, −1), −1 (−1, 0), −1	(0, −1), 0 (−1, 0), 0	(0, −1), +1 (−1, 0), +1
2	(−1, −1), −1	(−1, −1), 0	(−1, −1), +1

[a] The quantum state change is expressed as (m_1, m_2) in (a) and (b), where m_1 and m_2 show the ^{14}N quantum numbers during the evolution (t_1) and detection (t_2) periods, respectively. The quantum state change in (c) and (d) is expressed as ((m_{1A}, m_{1B}), m_{2A}), where m_{1A}, m_{1B}, and m_{2A} show the ^{14}N quantum numbers during t_1 of sites A and B and that during t_2 of site A, respectively.

for some typical torsion angles in the strong coupling limit. The dyad configuration (meso or racemo) and two successive backbone torsion angles between the relevant two ^{13}CN sites are specified in each spectrum in Figure 4. Parts b and c of Figure 4 show that $T'\bar{T}'$ and $T'T'$ conformations can be distinguished, as in the $^{13}CH_2$-aPAN spectra.[6] In addition, in the present experiment, $T'T'$ (160°, 160°) and $\bar{T}'\bar{T}'$ (−160°, −160°) can also be distinguished clearly, see Figure 4c,d, while their $^{13}CH_2$-DOQSY spectra are equivalent.[6]

The striking differences between DOQSY spectra of mTT and rTT dyads are demonstrated by Figure 4a,e. In other words, these dyads can be distinguished even if their conformations are the same, due to the different angles between the relevant two CN groups. The effects of deviations from exact 180° trans torsion angles in rTT dyads are displayed in Figure 4e−h. These are observed even more clearly in the $^2H-^{13}C$ correlation experiments described in the following paper.[22]

The comparison of Figure 4a,i demonstrates that trans and gauche conformations in meso dyads can also be distinguished by this experiment. Here, dyads that contain $\bar{G}$ and GG conformations are excluded, due to strong steric hindrance ($\bar{G}$ effect and pentane effect).[1,2] On the other hand, the spectra of rTT (Figure 4e) and mTG (Figure 4i) dyads look similar. In particular, the spectrum of the $mT\bar{G}$ dyad (not shown here) is exactly the same as that of the rTT dyad due to the geometric equivalence between the relevant pairs of C≡N bond orientations. However, these dyads can be distinguished by 2D DOQSY and DQ-filtered experiments on a $^{13}CH_2$-aPAN sample, which was demonstrated in our previous paper,[6] and by the $^2H-^{13}C$ 2D HMQC experiment on a 75% 2-^2H/25% 1-^{13}C-labeled aPAN sample shown in the following paper.[22] Note that, for these DOQSY patterns, the sequence of the two torsion angles is irrelevant. Thus, mTG and mGT dyads give identical patterns.

In the simulations, the triplet splitting due to the directly bonded ^{14}N has been taken into account. For 2D experiments involving dipolar-coupled $^{13}C-^{14}N$ spin systems, we should think about ^{14}N spin−lattice relaxation during the mixing period. In the present 2D DOQSY experiments, the sum of the DQ reconversion period (0.8 ms) and the z-filter period (2.0 ms) corresponds to the mixing period. The ^{14}N spin in the $^{13}C\equiv^{14}N$ group of site A can be in the three different states during the evolution t_1 period; $m_{1A} = -1, 0, +1$. If ^{14}N spin−lattice relaxation does not occur significantly between evolution and detection, the quantum state of the ^{14}N spin of site A during the acquisition t_2 period, m_{2A}, is the same as m_{1A}, and that of site B in t_1 is arbitrary, $m_{1B} = -1, 0, +1$. This results in the overlap of patterns from nine m states as shown in Table 1c. If ^{14}N spin−lattice relaxation occurs, m_{2A} is no longer necessarily the same as m_{1A}, resulting in the appearance of 15 states as shown in Table 1d. The effect of the ^{14}N spin−lattice relaxation can be monitored by 2D ^{13}C CSA exchange spectroscopy. The ^{14}N spin−lattice relaxation gives an exchange signal in a 2D ^{13}C CSA exchange spectrum even when no spin diffusion or molecular reorientation occurs (see Table 1a,b). An experimental 2D ^{13}C CSA exchange spectrum of our ^{13}CN-aPAN sample showed off-diagonal intensity due to the ^{14}N spin−lattice relaxation with an intensity of about 20% of the diagonal intensity after a mixing time of 5 ms. The duration of the present 2D DOQSY experiments is only 2.8 ms, with 0.8 ms of DQ reconversion and a 2.0 ms z-filter. In the following simulation, we neglect the small ^{14}N spin−lattice relaxation effect to reduce simulation times. In the simulated spectra, the nine patterns listed in Table 1c are summed up.

Although the overlap of the nine slightly different patterns arising from the $^{13}C\equiv^{14}N$ dipolar coupling somewhat smears out the 2D spectra, an angular resolution of 5−10° is attained, as demonstrated in Figure 4. This good angular resolution, which is due to the large CSA width and well-defined chemical shift tensor orientation of the $^{13}C\equiv N$ carbons, makes the following analyses of the torsion angle distribution reliable.

4.3.2. Experimental 2D DOQSY Spectrum. Figure 5a shows the experimental 2D DOQSY spectrum of ^{13}CN-aPAN in the strong coupling limit. The DQ coherence, $\omega_a + \omega_b$, in the ω_1 dimension is correlated with the single-quantum (SQ) CSA, ω_a or ω_b, in ω_2. The homonuclear dipolar coupling in the ω_2 dimension is much smaller than the CSA width as described above.

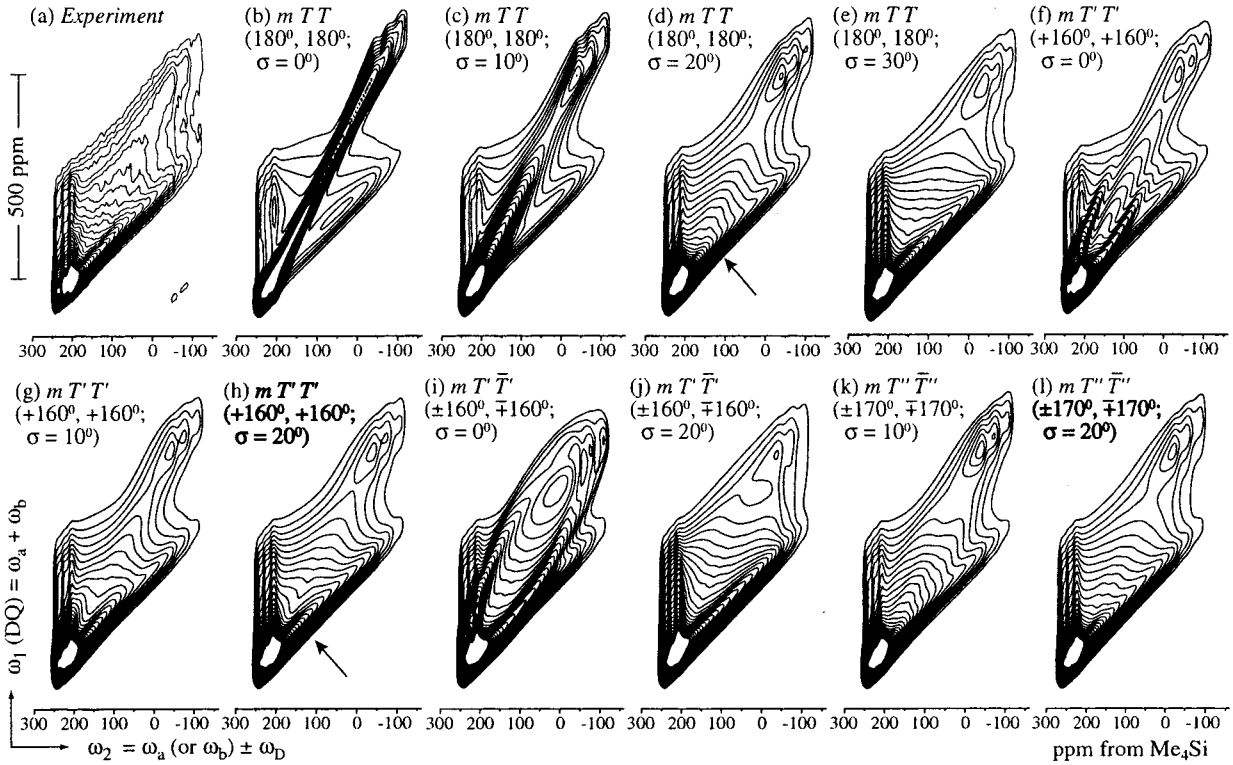

Figure 5. 2D DOQSY spectra of ^{13}CN-aPAN in the strong coupling limit with $\tau_{DQ} = 0.8$ ms. (a) Experimental spectrum. (b−l) Simulated spectra with various average torsion angles and their distributions for *mTT* dyads (indicated above each spectrum). Three contributions, *mTT*:*mTG*:*rTT* = 34:20:46 (meso:racemo = 54:46 and trans content 90%), are summed up, supposing that the *G* conformers are all part of the *mTG* dyads. The parameters for average torsion angles and distribution widths of (+170°, +70°; $\sigma = 10°$) and (180°, 180°; $\sigma = 10°$) were used for *mTG* and *rTT* conformations, respectively. Thirty contour lines are plotted between 2% and 60% of the maximum intensity. Other parameters are the same as in Figure 4.

The sample used here is atactic with meso:racemo = 54:46. Compared with the simulated spectra in Figure 4, the experimental spectrum is found to be made up mostly of the signals from *mTT* and *rTT* dyads, which give a straight line of slope two and straight ridges of slope one and parallel to the ω_1 axis, respectively. This predominance of trans conformations is confirmed quantitatively below.

4.3.3. Comparison of Experimental and Simulated 2D DOQSY Spectra. Parts b−l of Figure 5 show simulated spectra of ^{13}CN-aPAN for various *mTT* torsion angle distributions. From our previous work on a $^{13}CH_2$-aPAN sample, the trans:gauche ratio of aPAN was determined as 90%:10% (±10%). The 10% of gauche is believed to be contained almost exclusively in meso dyads.[7,14] Conformations containing *GG* or $\bar{G}$ are excluded due to the steric hindrance as described above. Thus, three contributions, *mTT*, *mTG*, and *rTT*, are superimposed in the simulation. Their ratios are (*mTT* + *mTG*):*rTT* = 54:46 and *mTT*:*mTG* = 34:20, which gives a trans content of 90%.

Under these conditions, the intensity near the diagonal of slope two reflects the conformation in *mTT* dyads exclusively. Compared with the simulated *mTT* spectra in Figure 4, the diagonal ridge near slope two in the experimental spectrum is significantly broader, indicating that the distribution of conformations of *mTT* dyads has a significant width. Thus, we applied a distribution of torsion angles, assuming a Gaussian distribution function. The parameter set (ψ_n, ψ_{n+1}; σ) is used in this paper for the description of the averages of two successive torsion angles (ψ_n, ψ_{n+1}) and the standard deviation σ of the Gaussian distribution of torsion angles. The Gaussian distributions for both torsion angles are presumed to have the same values of σ. For *TT* conformations, this is required for symmetry reasons. Conformations with distances of less than 2.52 Å between the relevant two ^{13}C sites in a ^{13}CN pair are not included in these simulations, because they are assumed to be energetically unfavorable. The torsion angle increment used in the simulations was 5°.

The discussion here is focused on the conformation of meso dyads. The spectrum of the *mTT* dyads is concentrated near the slope-two diagonal, and the distance between adjacent C≡N groups is mostly shorter for the *mTT* dyads, resulting in a more efficient excitation of their DQ coherence. Therefore, DOQSY patterns of the *mTT* dyads can be obtained quite selectively, and torsion angle distributions of the *mTT* dyads can be determined precisely. In contrast, DOQSY patterns of the *rTT* dyads overlap those of gauche-containing meso dyads as shown in Figure 4. The conformation of racemo dyads will be examined more accurately by ^{2}H−^{13}C 2D HMQC experiments in the following paper.[22] Here, the parameter sets (+170°, +70°; $\sigma = 10°$) and (180°, 180°; $\sigma = 10°$) are used for *mTG* and *rTT* dyads, respectively, and only the *mTT* parameters are varied in Figure 5.

The spectra for specific *mTT* conformations without distributions, e.g., (180°, 180°; $\sigma = 0°$), (+160°, +160°; $\sigma = 0°$), and (±160°, ∓ 160°; $\sigma = 0°$) in Figure 5b,f,i, show a clear diagonal ridge of slope two, or elliptical ridges. In the experimental spectrum, these clear ridges are not observed and the diagonal ridge of slope two is significantly broader. This confirms that the conforma-

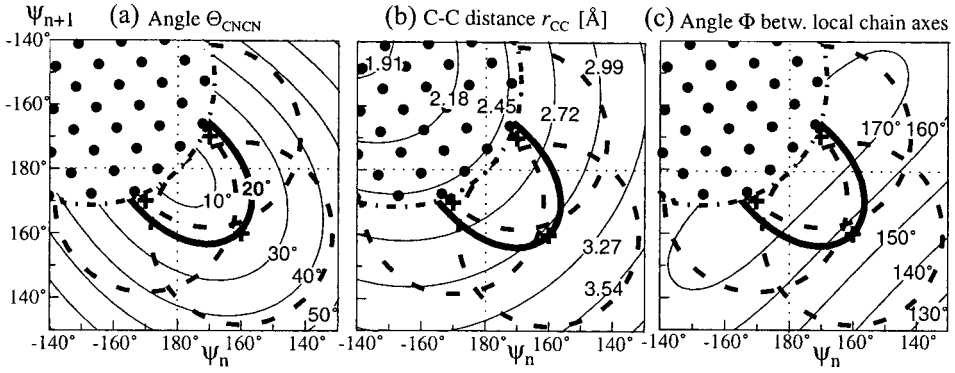

Figure 6. Expansion of the trans−trans regions of three geometrical maps of aPAN in the meso dyads (compare Figure 2). (a) Angle Θ_{CNCN} between C≡N bonds in adjacent side groups. As in Figure 2, the excluded region of close C−C contacts is marked by dots, and by a dashed−dotted demarcation line. The line of $\Theta_{CNCN} = 20°$ is marked in bold; average torsion angles on this line give the best fits to the experimental DOQSY spectrum. The widths of the distributions obtained from the best fits of the experimental spectrum are indicated by large dashed circles. These features are reproduced in the following plots. (b) Intramolecular four-bond C−C distance r_{CC} of adjacent C≡N side groups (Å), with the bold line of best-fit solutions superimposed. (c) Angle Φ between local chain axes on both sides of the relevant two backbone bonds.

tion of *mTT* dyads is distributed as suggested above, which is in agreement with the model of Rizzo et al.[7]

For the rest of Figure 5, Gaussian distributions of torsion angles are used. Parts c and d of Figure 5 have been obtained using Gaussian distributions of the trans torsion angles with $\sigma = 10°$ and $\sigma = 20°$, respectively, for the ideal *mTT* conformation (180°, 180°). The distribution with 20° gives a better match, but this shows less intensity at the ridge of slope one, indicated by an arrow in Figure 5d. Figure 5h shows the simulation with the *mTT* torsion angle set of (+160°, +160°; $\sigma = 20°$). This simulated spectrum nicely reproduces the experimental data including the intensity marked by the arrow in Figure 5h. While the spectrum of (±160°, ∓160°; $\sigma = 20°$) in Figure 5j shows a significant deviation from the experimental spectrum, the spectrum of (±170°, ∓170°; $\sigma = 20°$) in Figure 5l is mostly indistinguishable from that of (+160°, +160°; $\sigma = 20°$). A more detailed discussion of these two conformations will be given below. Spectra with Gaussian distributions of $\sigma = 10°$ or $\sigma = 30°$ are inconsistent with the experimental spectrum, as are those with torsion angle deviations of less than 10° and more than 30° from the exact (180°) trans state. The spectrum of (+160°, +160°; $\sigma = 10°$) (Figure 5g) shows a narrower ridge of slope two than the experimental spectrum. The three spectra obtained for (±170°, ∓170°; $\sigma = 10°$) (Figure 5k), (+170°, +170°; $\sigma = 10°$), and (±160°, ∓160°; $\sigma = 10°$) (not shown here) are significantly different from the experimental spectrum. The uncertainties in the determinations of the average torsion angles and of σ are estimated to be less than ±5 or 10°, depending on the torsion angle dependence of the CN−CN angles as shown in Figures 2c and 6a.

The *mTT* conformations of (+160°, +160°; $\sigma = 20°$) and (±170°, ∓170°; $\sigma = 20°$) give the best-fit 2D DOQSY spectra as shown above. The geometrical maps of Figure 2c and, more clearly, Figure 6a show that the average torsion angles (ψ_n, ψ_{n+1}) = (+160°, +160°) and (±170°, ∓170°) correspond to similar CN−CN angles of $\Theta_{CNCN} = 20°$. In principle, these conformations can be distinguished by ^{13}C 2D DOQSY experiments even for similar CN−CN angles, because the spectral patterns depend also on the ^{13}C−^{13}C distance and the ^{13}C−^{13}C vector direction of the two relevant sites. Parts c and d of Figure 4 are examples of spectra that differ even though they have similar CN−CN angles. However, the spectra with *mTT* conformations of (+160°, +160°; $\sigma = 20°$) and (±170°, ∓170°; $\sigma = 20°$) are practically indistinguishable, because spectral differences in this relatively small angular region are smeared out by various factors, such as the splittings due to ^{13}C−^{14}N dipolar couplings and the torsion angle distributions. This means that, to a good approximation, the 2D DOQSY spectra of the ^{13}CN-aPAN sample are determined only by the CN−CN angles. Therefore, all conformations on the line of $\Theta_{CNCN} = 20°$ in the allowed region of Figure 6a are candidates for *mTT* conformations in aPAN. Nevertheless, in the following the discussion can be limited mostly to the two extremes (ψ_n, ψ_{n+1}) = (+160°, +160°) and (±170°, ∓170°), which according to Figure 6b have the longest and nearly shortest ^{13}C−^{13}C distances, respectively, in this limited region.

Figure 6b shows that the adjacent C≡N groups in *mTT* dyads are in closer proximity for (±170°, ∓170°; $\sigma = 20°$). Thus, the conformation of (+160°, +160°; $\sigma = 20°$) alleviates the steric hindrance and the large electric dipole interaction between the C≡N groups, which lowers the intramolecular conformational energy further. On the other hand, aPAN is a laterally ordered polymer whose chains are packed in a pseudohexagonal form. Thus, from the viewpoint of the crystal structure of aPAN, the conformation (±170°, ∓170°; $\sigma = 20°$) would be more suitable for laterally ordered packing, because the local chain axes are close to parallel (see Figure 6c). From the comparison with conformational calculations in section 4.4 below, it appears likely that *mTT* dyads take both conformations depending on adjacent configurations.

4.3.4. Determination of the Trans Content. In our previous work, the trans content was determined to be 90% (±10%).[6] Here, we can utilize the ^{13}CN-aPAN spectra to check the trans content of aPAN again. Parts b and c of Figure 7 show simulations with trans contents of 80% and 100%, respectively. The other parameters are the same as for the simulation of Figure 5h. In Figure 8, the sum projections onto the ω_2(SQ) and ω_1(DQ) axes are shown at the top and bottom of each

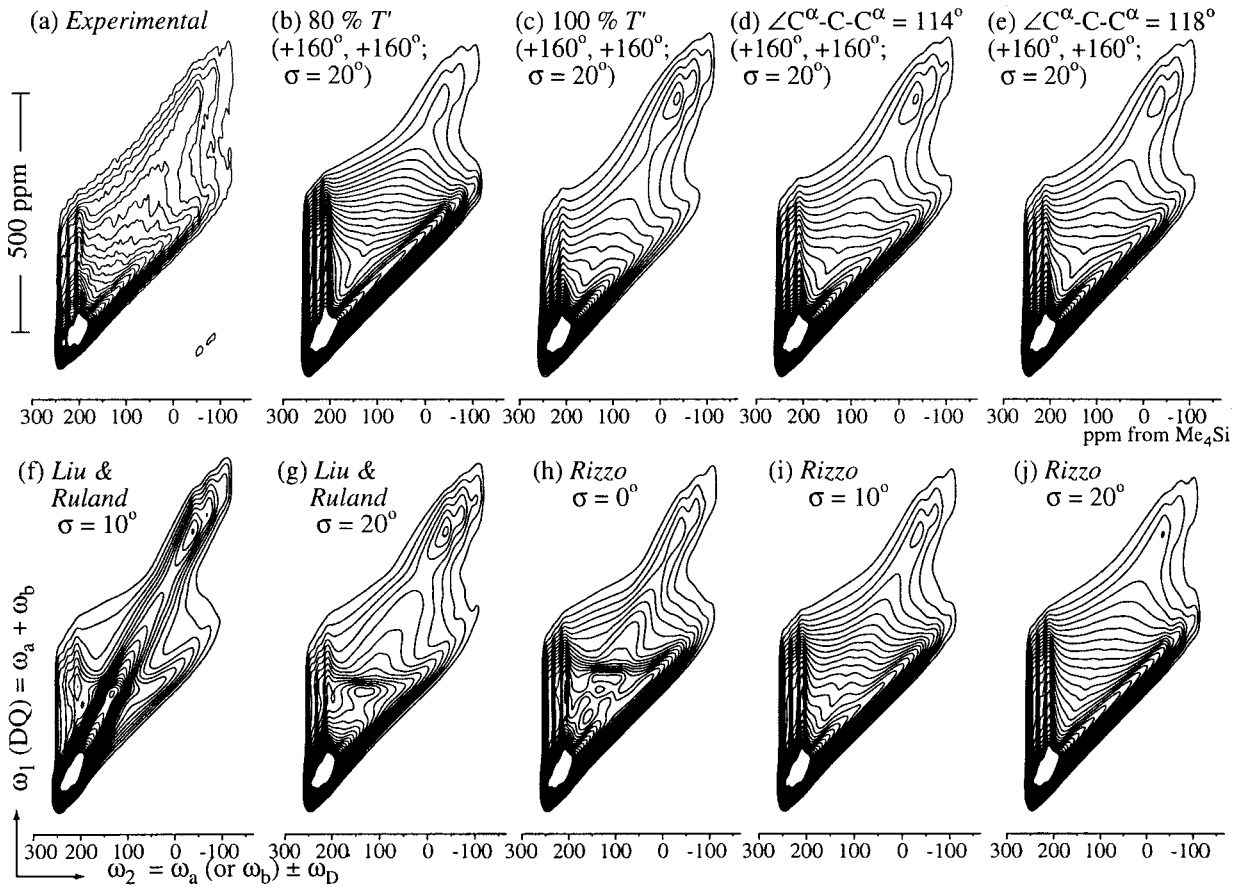

Figure 7. Dependence of simulated 2D DOQSY spectra on trans content (b, c) and valence bond angles in the backbone (d, e). The relevant parameters are shown above each spectrum. All the other parameters for simulation and plotting are the same as in Figure 5. The experimental spectrum is shown in (a) for reference. (f−j) Simulated spectra of ^{13}CN-aPAN based on a model by Liu and Ruland (f, g), and on a model by Rizzo et al. (h−j). In (f) and (g), three contributions, *mTT*:*mTG*:*rTT* = 34:20:46, have been summed up. The ideal torsion angles of 180° and +60° are used for *T* and *G*, respectively. Gaussian distributions with σ = 10° and 20° have been applied only for mTT dyads for (f) and (g), respectively. In (h−j), minimum-energy extended conformations with various torsion angles as listed by Rizzo et al. in Tables 3−5 of ref 7 have been summed up with the weighting factors calculated from each conformational energy. The meso:racemo ratio is 54:46, and the trans:gauche:anticlinal ratio is 75:20:5. The applied Gaussian distributions, σ, for (h), (i), and (j) are 0°, 10°, and 20° for all contributions, respectively. Other parameters are the same as in Figure 5.

figure, respectively. The 2D DOQSY spectra in Figures 5 and 7 and DQ sum projection spectra in Figure 8 clearly show that the trans contents of 80% and 100% over- and underestimate the *mTG* content, respectively. This confirms our previous result on the trans content of 90%; the experimental error is now estimated to be ±5%.

It may be surprising that the ^{13}CN-aPAN DOQSY spectrum is even more sensitive to the trans content than the $^{13}CH_2$-aPAN DOQSY spectrum of ref 6. The main reason is that only the *mTT* dyad contributes to the diagonal ridge of slope two in the 2D ^{13}CN-aPAN spectrum and the corresponding broad component, with a peak on the left, in the DQ sum projections of Figure 8. Since we have neglected the contribution of $\bar{G}$- and *GG*-containing conformations in both dyads, and *G*-containing conformations in racemo dyads as described above, the ratios of all the relevant conformations are given by

$$mTT{:}mTG{:}rTT = (54 - 2x){:}2x{:}46 \qquad (7)$$

where *x* is the gauche content (%). For the $^{13}CH_2$-aPAN spectrum, the *TT* conformations of both meso and racemo configurations contribute to the diagonal ridge. The diagonal intensity of the $^{13}CH_2$-DOQSY spectrum for a gauche content of 20% is 100 − (2 × 20) = 60% of that without a gauche conformation. In contrast, the diagonal intensity of the ^{13}CN-DOQSY spectrum with a gauche content of 20% is reduced to 100 × (54 − (2 × 20))/54 = 26% of that without a gauche conformation, because only the *mTT* conformation contributes to the diagonal ridge. This shows that the diagonal intensity in the present DOQSY experiment on the ^{13}CN-aPAN sample changes more strongly with the trans/gauche ratio.

4.3.5. Effect of the Backbone Valence Angle. The backbone valence angle, ∠C$^{\alpha}$CC$^{\alpha}$, is another parameter in the simulations. In RIS models, the angles ∠C$^{\alpha}$CC$^{\alpha}$ for the *TG* conformation of vinyl polymers are assumed to be 112−117°, as is shown in Tables VIII-2 and VIII-3 of ref 2. Parts d and e of Figure 7 show simulations with ∠C$^{\alpha}$CC$^{\alpha}$ = 114° and 118°, respectively. The other parameters are the same as for the simulation of Figure 5h, where ∠C$^{\alpha}$CC$^{\alpha}$ = 109.5°. It is found that the intensity at $\sigma_{\parallel}$, the upfield (low-intensity) end of the spectrum, becomes smaller with increasing valence angle ∠C$^{\alpha}$CC$^{\alpha}$. The $\sigma_{\parallel}$ intensity in the experimental spectrum is consistent with a backbone bond angle in the range of 109.5−114°.

4.4. Torsion Angles of *mTT* Dyads: Comparison with Previous Investigations. Hobson and Windle,[8]

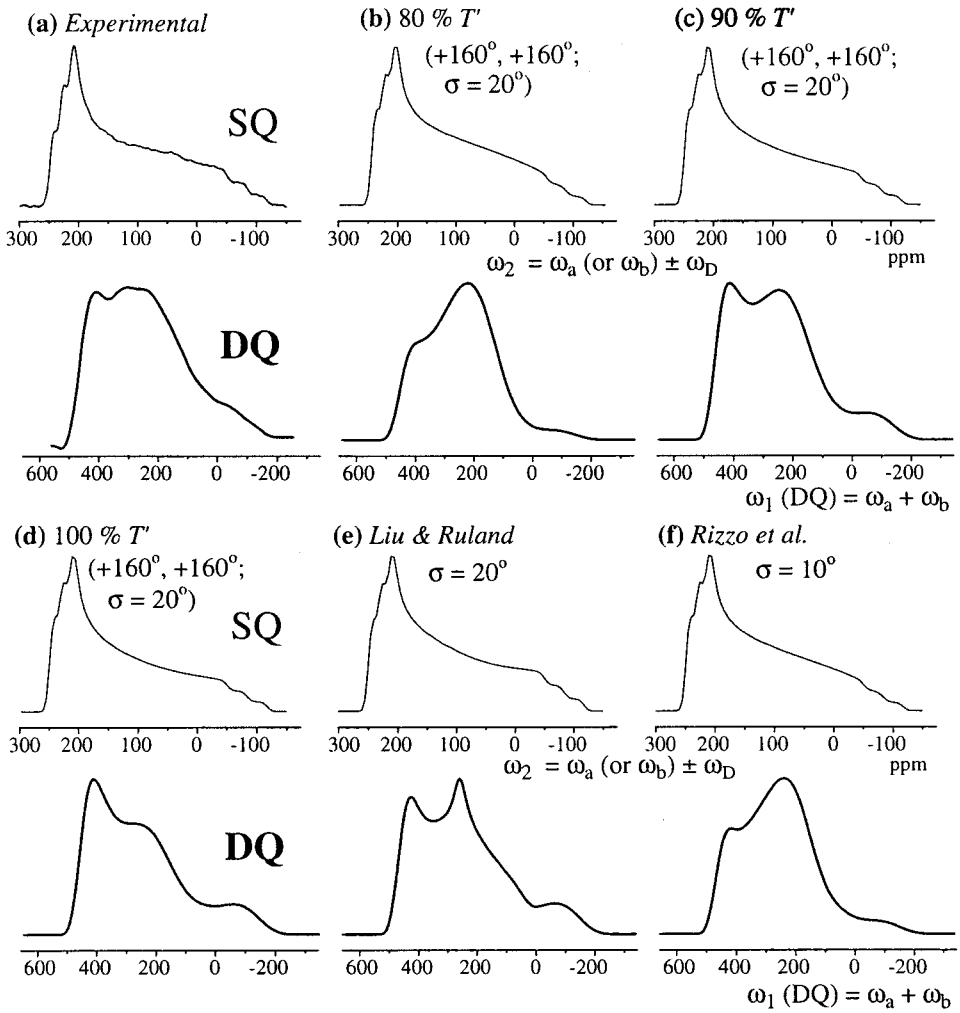

Figure 8. Sum projections of 2D DOQSY spectra onto the ω_2(SQ) and the ω_1(DQ) axes. (a) Projections of the experimental 2D spectrum. (b−d) Simulated projections for trans contents of 80%, 90%, and 100%, obtained from the 2D spectra in Figures 7b, 5h, and 7c, respectively. (e) Simulated projections based on the model by Liu and Ruland, obtained from the 2D spectrum in Figure 7g. (f) Simulated projections based on the model by Rizzo et al., obtained from the 2D spectrum in Figure 7i.

and Rizzo et al.[7] reported that the conformational energy minimization procedures for isotactic (all-*m*) PAN model chains resulted in conformations around (±160°, ∓160°) as energetically feasible straight chains (see Table 5 in ref 8 and the bottom of Table 3 in ref 7). (Note that the definition of torsion angle signs, + and −, in refs 7 and 8 is different from ours, and the signs have been converted to our convention in this paper.) In contrast, the conformational energy minimization procedure for meso dyads in a *rrrmrr* heptad sequence resulted in a conformation around (+170°, +170°) for all-trans extended chains (lines A of Table 4 in ref 7) even though torsion angles near (±160°, ∓160°) were used in the starting conformation for the calculation. The meso dyads in a *rrmmrr* heptad sequence also resulted in a conformation around (+170°, +170°), although the successive torsion angles are not for $C^{\alpha}-C-C^{\alpha}$ but for $C-C^{\alpha}-C$ (line A of Table 5 in ref 7). These results suggest that both conformations (+160°, +160°; $\sigma = 20°$) and (±170°, ∓170°; $\sigma = 20°$) are possible in the actual aPAN sample, although the average torsion angles and their distributions obtained from our experiments do not quantitatively agree with those from the calculations in the literature. The conformation of (+160°, +160°; $\sigma = 20°$) appears likely when the relevant meso dyad is bonded to one or two racemo dyads, while the conformation of (±170°, ∓170°; $\sigma = 20°$) looks favorable when the relevant meso dyad is bonded to meso dyads on both sides. Even though the 2.56 Å distance between the adjacent CN carbons in the (±170°, ∓170°) conformation is quite short, this conformation could be attained because otherwise the polymer chain tends to bend. The distances between adjacent C≡N carbons and the angles of local chain axes for all the above-mentioned candidates for *mTT* conformations are between the two extremes of (ψ_n, ψ_{n+1}) = (+160°, +160°) and (±170°, ∓170°). Therefore, all of these conformations should be considered as possible in *mTT* dyads of aPAN.

The experimental 2D DOQSY spectrum of a ^{13}CN-aPAN sample (Figure 7a) can be directly compared to simulated spectra based on models by Liu and Ruland[14] (Figure 7f,g) and Rizzo et al.[7] (Figure 7h−j). In the model proposed by Liu and Ruland, an aPAN chain consists of a planar zigzag conformation with 1 kink per 10 monomer units, which gives a gauche content of 10%. Thus, three types of dyads, *mTT*, *mTG*, and *rTT*, are superimposed with a ratio of 34:20:46, which results in meso:racemo = 54:46 and trans:gauche = 90:10. The ideal torsion angles, 180° for *T* and +60° for *G*, are used. Figure 5b has shown that, without distributions of torsion angles, the diagonal ridge of slope two is sharper than in the experimental spectrum, indicating that the torsion angles of *mTT* dyads should be distributed. In

the spectra of Figure 7f,g, Gaussian distributions with $\sigma = 10°$ and 20°, respectively, have been applied for the *mTT* dyads in Liu and Ruland's model. Even with a wide distribution, the average torsion angles of (180°, 180°) in Liu and Ruland's model are not appropriate, as was shown in our detailed analysis of Figure 5b−e.

The spectra in Figure 7f,g give distinct elliptical off-diagonal patterns, indicating that distributions should be introduced for the *rTT* dyads as well. This is also seen in the sum projection of the spectrum of Figure 7g onto the DQ axis; see Figure 8e. The sharp horn in the 1D DQ sum projection at about 240 ppm originates mainly from the well-defined single conformation of the *rTT* dyads. This distribution is probed even more directly by $^2H-^{13}C$ correlation NMR in our companion paper.[22] The distribution in the *mTG*/*mGT* dyads cannot be determined from our DOQSY spectra, mostly due to the low concentration of these conformations. However, we assume them to be similarly distributed as the *rTT* dyads; there is no reason to assume that only *mTG*/*mGT* dyads should have a specific well-defined conformation. In our $^2H-^{13}C$ correlation study,[22] we see strong evidence that the *mGT* dyads indeed have a significant distribution width. The spectral patterns are also insensitive to the ratio of *TG* and $T\bar{G}$, and any kind of ideal kink defects (not shown here).

Hobson and Windle[8] have proposed *mTT* conformations around (±160°, ∓160°). These are inconsistent with our experimental spectrum. The simulated 2D DOQSY spectra for these conformations, see Figure 5i,j, exhibit depressions along the slope-two diagonal, while the experimental spectrum shows a broad ridge.

For the 2D DOQSY simulations based on the model by Rizzo et al.,[7] dyads with minimum-energy extended conformations in Tables 3−5 of ref 7 have been summed up with the weighting calculated from the corresponding conformational energies. The meso:racemo ratio is 54:46, and the trans:gauche:anticlinal ratio is 75:20:5. The results are shown in Figure 7h. As stated in ref 7, the conformation sets in their Tables 3−5 represent not all but only some typical conformations. Therefore, further Gaussian distributions of torsion angles with $\sigma = 10°$ and 20° were introduced in the simulations shown in Figure 7i,j, respectively. These spectra are similar to the simulation of Figure 7b, where the trans content is 80%. The sum projections for Figure 7i are shown in Figure 8f; as expected, they also resemble those in Figure 8b (80% trans), while the best fit to the projection of the experimental spectrum was obtained with 90% trans. This shows that the trans content is underestimated in the model by Rizzo et al.

In summary, our experimental 2D DOQSY spectrum can be explained by a model that combines the ratio of trans:gauche = 90:10 in the model by Liu and Ruland with the torsion angle distribution suggested by the calculations of Rizzo et al.

5. Conclusions

We have investigated the torsion angle distribution of meso dyads in laterally ordered atactic PAN by ^{13}C 2D DOQSY on a $^{13}C{\equiv}N$-labeled aPAN sample. The large CSA widths of the $^{13}C{\equiv}N$ carbons provide good angular resolution in the NMR experiment, and the well-defined chemical shift tensor orientation has enabled us to determine the torsion angles accurately. High-quality DOQSY spectra were obtained even for the large CSA width of the sp-hybridized nitrile carbon, by incorporating a frequency-switching technique into the DOQSY pulse sequence. It provides complete separation of the DQ spectrum from single- and zero-quantum artifacts, while all pulses, including the 180° pulses in an *xy*-16 sequence during the DQ excitation and reconversion periods, are applied on-resonance.

The average torsion angles in meso trans−trans dyads have been found to deviate by 10−20° from the ideal trans conformation, and the torsion angles are widely distributed with a standard deviation $\sigma = 20 \pm 5°$. Typical average torsion angles are (+160 ± 10°, +160 ± 10°) and (±170 ± 5°, ∓170 ± 5°). The adjacent CN−CN angles, Θ_{CNCN}, for these conformations are ∼20° on average, and intermediate conformations between the mentioned typical average torsion angles with $\Theta_{CNCN} = 20°$, see the bold line in Figure 6, are also consistent with the NMR data. Judging from conformational calculations, most conformations with $\Theta_{CNCN} \approx 20°$ must be considered as possible in meso trans−trans dyads of aPAN, except for those with C−C distances in adjacent C≡N groups that are shorter than the ∼2.52 Å distance in the ideal trans state.

This NMR study is the first experiment to determine, quantitatively, the torsion angle deviations from the ideal trans state in meso trans−trans dyads in aPAN and the torsion angle distributions in meso trans−trans dyads. These torsion angle deviations and distributions permit the formation of the laterally ordered crystalline structures proven by WAXD patterns of oriented aPAN fibers, despite large steric and electrostatic interaction between C≡N groups. It is also confirmed that the trans:gauche ratio of backbone bonds in aPAN is 90:10 (±5%), in agreement with our previous DOQSY NMR investigation of a $^{13}CH_2$-aPAN sample.

Acknowledgment. H.K. thanks the International Fellowship by the Ministry of Education, Science, Sports and Culture, Japan, for financial support. K.S.-R. thanks the National Science Foundation (Grant DMR 9703916) for funding this work and NSF/MRSEC for support of the NMR facility.

6. Appendix. Off-Resonance Evolution with On-Resonance Pulses in 2D NMR Experiments

In this Appendix, a frequency-switching technique for markedly improving the quality of DOQSY spectra and other 2D powder patterns is presented. It is shown that off-resonance evolution can be achieved while all pulses are applied on-resonance, by simply switching the frequency off-resonance exclusively during the evolution time t_1. In 2D DQ spectroscopy of static solids, the on-resonance pulses minimize excitation problems, while switching the frequency off-resonance by tens of kilohertz in ω_1 permits complete separation of the DQ powder pattern from zero-quantum (ZQ) and single-quantum (SQ) artifacts. A version of the experiment that cleanly compensates for effects of finite frequency-switching times using a Hahn echo and positive/negative switches is also presented.

6.1. Motivation for Applying Frequency-Switching. In 2D DOQSY experiments, undesired ZQ and SQ coherences in ω_1 are to be suppressed by extensive phase cycling. For the broad powder patterns of sp^2- and sp-hybridized carbons, the outer regions of the spectrum are often 10 kHz or more off-resonance, and the resulting pulse imperfections lead to the appearance of ZQ and SQ artifacts. While the 2D DQ patterns are often

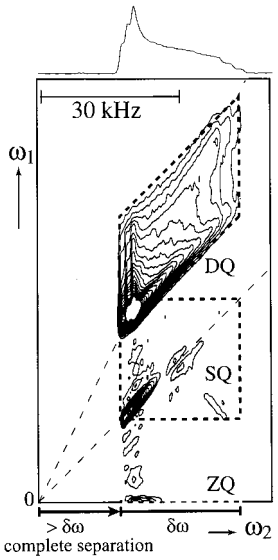

Figure 9. Experimental 2D DOQSY spectrum of ^{13}CN-aPAN, including the SQ and ZQ artifacts. The ^{13}C frequency was switched off-resonance by 30 kHz during the t_1 evolution time. All the pulses were applied at a frequency near the center of the powder spectrum. The dashed lines outline the regions in which signal can appear. Complete separation of the DQ and SQ regions requires moving off-resonance from the nearest edge of the spectrum by more than the full width $\delta\omega$ of the powder spectrum. Note that the on-resonance frequency during detection ($\omega_2 = 0$) is that of the pulses and therefore within the region of spectral intensity. The DQ spectrum here is the same as that in Figures 5a and 7a except for the contour levels. Of 40 contour lines, 20 are plotted between 3% and 60% of the maximum intensity, and 20 between −3% and −60% to show the ZQ and SQ artifacts, which are mostly negative. The integral projection of the 2D spectrum is shown at the top.

broad in both dimensions and therefore of small height, ZQ and SQ signals in ω_1 have significant heights because they are usually sharp; they trivially correlate the frequency ω_2 with $\omega_1 = 0$ and with itself, $\omega_1 = \omega_2$, which produces a sharp zero-frequency and diagonal ridge, respectively. As a result, even at small integral intensities, the ZQ and SQ artifacts will be disproportionately high relative to the broad DQ patterns. If the spin−spin relaxation time, T_2, is long and the anisotropy large, the height of these artifacts is up to 30% of the maximum double-quantum signal. Even time-consuming parameter optimization and good spectrometer stability may not ensure complete suppression of these artifacts. As $\mathbf{B}_0$ field strengths and consequently chemical shift anisotropies continue to increase, this problem will become more and more acute.

A relatively simple solution to this problem is provided by off-resonance evolution, since the doubled off-resonance shift of double-quantum coherences[21,26−29] separates them from the ZQ and SQ artifacts (see Figure 9). Off-resonance evolution, i.e., evolution with the carrier frequency outside the region of spectral intensity, also makes it possible to restrict the data to a single cosine data set. This is less complicated than other schemes for solving the two-dimensional phase problem, which are otherwise, in terms of signal-to-noise ratio and data storage, completely equivalent.[30]

DQ spectra for aliphatic carbons have been successfully recorded by applying the pulses flanking the evolution period off-resonance.[3−5,19] However, for sp^2- or, in particular, sp-hybridized carbon species such as the C≡N group in PAN, a clean separation of the DQ

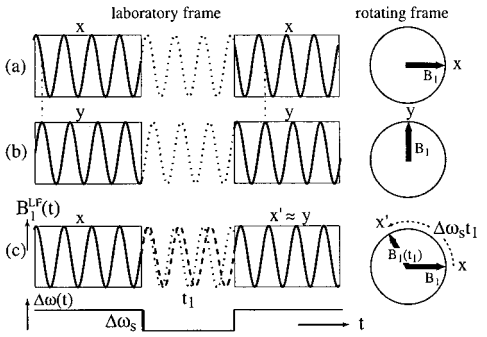

Figure 10. Principle of off-resonance evolution with on-resonance pulses. The pulse sequences are (a) x, t_1, x; (b) y, t_1, y; and (c) x, frequency switch, t_1, frequency switch, x'. (a) and (b) are reference pulse sequences without frequency switch; they help to show that the phase of the pulse x' is close to that of the y-pulse. The radio frequency field $\mathbf{B}_1^{LF}(t)$ in the laboratory frame is shown on the left and the $\mathbf{B}_1$ field viewed in the original (on-resonance) rotating frame on the right. Note that the ratio of the oscillation period to the pulse length is strongly exaggerated, given that, at 75 MHz, there are 75 oscillations/μs.

coherences from the artifacts requires the evolution to be off-resonance by tens of kilohertz due to the large CSA. The DQ spectrum of ^{13}CN-aPAN, measured by the pulse sequence with the frequency switches, is shown in Figure 9 with ZQ and SQ artifacts. It is found that a complete separation of the DQ signals from the SQ signals requires moving off-resonance from one edge of the spectrum by at least a full width $\delta\omega$ of the spectrum. Applying radio frequency pulses so far off-resonance degrades the signal intensity and phase behavior of the double-quantum spectra to an unacceptable degree. In the following, it is shown how off-resonance evolution with on-resonance pulses can be achieved simply by switching the spectrometer frequency off-resonance during the evolution period t_1, i.e., only during a time in which no pulses are applied.

For obtaining the spectrum of Figure 9, the ^{13}C frequency was switched 30 kHz off-resonance during the t_1 evolution time. The sequence of frequencies in Figure 11b, with respect to the on-resonance frequency, was 0 kHz (on-resonance)−(−30 kHz)−(+30 kHz)−t_1−(0 kHz). The switching times can be optimized using a frequency-switched stimulated-echo pulse sequence, with the same Hahn echo and frequency-switch around t_1 before the mixing time as shown in Figure 11b. The signal observed for $t_1 = 0$ is modulated by $\cos(\phi')$, where ϕ' is the accumulated phase during the switches (see below). When the signal has been maximized by varying the switching times, the condition of $\phi' = 0$ has been identified.

6.2. Theory. 6.2.1. Effect of an Off-Resonance Frequency Switch between On-Resonance Pulses. The effect of switching the radio frequency off-resonance and back on-resonance between pulses is not completely trivial. It is widely believed that switching of the spectrometer frequency to a different value just during a window t_1 between pulses, while applying all pulses at the initial frequency, will not have an observable effect. However, transverse magnetization and coherences in fact acquire an additional phase due to the frequency switch, as will be shown in the following.

Normally, NMR experiments are described in a frame rotating with the pulses. When the frequency is switched by $\Delta\omega_s$ during the time t_1 as shown in Figure 10c, two rotating frames can be considered, which rotate with

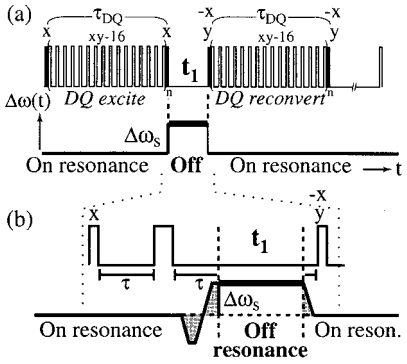

Figure 11. (a) Detailed description of the DQ pulse sequence around the t_1 evolution period, with idealized, nearly instantaneous frequency switch. The *xy*-16 sequence of 180° pulses[16,17] is applied during DQ excitation and reconversion to keep the spin system in the strong coupling limit. (b) Pulse scheme to be used for significant switching times (>1.5 μs). A Hahn echo (with the 180° pulse still on-resonance) provides time for switching. For easy phase correction in the ω_1 dimension, the total gray area under the $\Delta\omega(t)$ curve, which is proportional to the total phase at $t_1 = 0$, should be zero, due to cancellation of its positive and negative portions.

respect to each other by $\Delta\omega_S$. We will describe the situation consistently in the first ("original", "on-resonance") frame, as shown on the right-hand side in Figure 10. As a result of the $\Delta\omega_S$ rotation of the switched-frequency rotating ("off-resonance") frame with respect to the original one, the $\mathbf{B}_1$ field of an *x*-pulse applied at the end of t_1 (denoted as x' in Figure 10c) will make an angle $\phi = \Delta\omega_S t_1$ with the $\mathbf{B}_1$ field of an *x*-pulse before the frequency switch. This relation holds not only if the *x*-pulse is applied while the frequency stays off-resonance. It also applies after the frequency is switched back on-resonance, since the frequency switch does not change the direction of $\mathbf{B}_1$ instantaneously, but only linearly with time.

This is confirmed by a consideration in the laboratory frame, where the frequency switch leads to a linear increase $\Delta\omega_S t_1$ in the relative phase between the original and the new oscillating radio frequency field strength $\mathbf{B}_1{}^{LF}(t)$; see Figure 10c. This phase increase corresponds to a linear increase in the angle between the original and the new $\mathbf{B}_1$ field direction in the original rotating frame.

As a result of the rotation of the *x*-direction by $\phi = \Delta\omega_S t_1$, the magnetization at the end of t_1 makes an angle of $-\phi = -\Delta\omega_S t_1$ with the storage pulse(s) (in addition to the phase $\tilde{\omega}_1 t_1$ acquired in the on-resonance rotating frame). In contrast, double-quantum coherence evolves with twice the off-resonance frequency.[21] More specifically, the relevant double-quantum coherence ($S_x L_y + S_y L_x$) evolves during t_1 with the sum of the chemical shift and off-resonance frequencies ω_S and ω_L of the two coupled spins *S* and *L*, each measured relative to the frequency of the pulses. The extra phase $\phi = \Delta\omega_S t_1$ of the $\mathbf{B}_1$ field at the start of DQ reconversion will affect both *S* and *L*, each by an angle $-\phi$:

$$\begin{aligned}\rho(t_1) &= [S_x \cos(\omega_S t_1 - \phi) + S_y \sin(\omega_S t_1 - \phi)] \\ &\quad [L_y \cos(\omega_L t_1 - \phi) - L_x \sin(\omega_L t_1 - \phi)] \\ &\quad + [S_y \cos(\omega_S t_1 - \phi) - S_x \sin(\omega_S t_1 - \phi)] \\ &\quad [L_x \cos(\omega_L t_1 - \phi) + L_y \sin(\omega_L t_1 - \phi)] \\ &= (S_x L_y + S_y L_x) \cos(\{\omega_S + \omega_L\} t_1 - 2\Delta\omega_S t_1) \\ &\quad + (S_y L_y - S_x L_x) \sin(\{\omega_S + \omega_L\} t_1 - 2\Delta\omega_S t_1) \quad \text{(A1)}\end{aligned}$$

This shows the expected doubled off-resonance shift of $-2\Delta\omega_S$.

6.2.2. Relationship to Time-Proportional Phase Shifts. The simple scheme described here has a close analogy to time-proportional phase incrementation (TPPI) as applied, for instance, in multiple quantum (MQ) spin-counting experiments.[26−29] There, the phase of the pulse is systematically incremented with t_1, $\phi = \Delta\omega_S t_1$. Like the frequency switch, this results in the magnetization being rotated, with respect to the pulses after t_1, by an angle $-\Delta\omega_S t_1$ around the *z*-direction. For an *N*-quantum coherence, by definition this generates a modulation by $-N\Delta\omega_S t_1$.[21,26−29] Thus, the MQ coherence orders can be separated in ω_1. The frequency-switch experiment has the advantage that it can be performed with simple and fast quadrature pulses available on almost all spectrometers.

6.3. Compensation of Finite Switching Times. Sometimes, in particular with older spectrometers, the frequency switch is too slow to be considered as instantaneous. The switching delay would introduce serious dead-time problems if the simple frequency-switching pulse scheme of Figure 10c or 11a was used. The combination of a Hahn echo and positive/negative frequency switches can avoid this problem as shown in Figure 11b. By performing the switches in the second τ-period of a Hahn echo sequence $\tau-180°-\text{pulse}-\tau$, the chemical shift evolution effects outside t_1 are removed. The phase acquired by the $\mathbf{B}_1$ field in the original rotating frame is

$$\phi' = \int_0^\tau \Delta\omega(t)\, dt \quad \text{(A2)}$$

The phase acquired by switching to $\Delta\omega_S$ can be compensated by a short switch to $-\Delta\omega_S$, as indicated in Figure 11b. The total phase ϕ', which is equal to the area under the $\Delta\omega(t)$ curve as indicated by gray shading in Figure 11b, should vanish at $t_1 = 0$. Otherwise, the data have a constant phase error in the first dimension.

The pulse sequence with a Hahn echo also permits us to introduce dipolar dephasing of DQ coherence involving protonated carbons, as shown in Figure 1. This can remove undesirable aliphatic signals, which even in natural abundance produce ridges that are detectable due to the small CSA width of these sites.

6.4. Phase Stability. In the experiment, phase stability of the radio frequency during the switch is required. In terms of $\mathbf{B}_1{}^{LF}(t)$ in Figure 10c, this means that no uncontrolled changes in $\mathbf{B}_1{}^{LF}(t)$ occur. In other words, it keeps changing with the instantaneous frequency $\omega_{RF}(t)$ according to

$$\mathbf{B}_1{}^{LF}(t) = \mathbf{B}_1{}^{LF}(0) \cos[\int_0^t \omega_{RF}(t')\, dt'] \quad \text{(A3)}$$

Phasing stability has been provided on commercial spectrometers for nearly two decades (at least for switches by less than 10 kHz), since it is also necessary for various other NMR techniques, such as frequency-switched Lee−Goldburg decoupling.[31,32] On modern spectrometers, switches by tens of kilohertz can be performed reliably within a few microseconds.

6.5. Perspective on the Frequency-Switching Technique. In this Appendix, we have shown that off-resonance evolution with all pulses on-resonance is possible and enables the measurement of broad DQ patterns free of ZQ and SQ artifacts, far off-resonance in ω_1. The principle of frequency-switching is general

and can be applied in the evolution period(s) of almost any multidimensional experiment. It may prove especially valuable in three-dimensional NMR, where measuring a single data set, $\langle \cos \tilde{\omega}_1 t_1 \cos \tilde{\omega}_2 t_2 \exp(i\tilde{\omega}_3 t_3) \rangle$, off-resonance is particularly advantageous for simplicity of data processing.

References and Notes

(1) Flory, P. J.; Jackson, J. G.; Wood, C. J. *Statistical Mechanics of Chain Molecules*, 2nd ed.; Oxford University Press: New York, 1989.
(2) Mattice, W. L.; Suter, U. W. *Conformational Theory of Large Molecules: The Rotational Isomeric State Model in Macromolecular Systems*; Wiley: New York, 1994.
(3) Schmidt-Rohr, K.; Hu, W.; Zumbulyadis, N. *Science* **1998**, *280*, 714.
(4) Dunbar, M. G.; Novak, B. M.; Schmidt-Rohr, K. *Solid State Nucl. Magn. Reson.* **1998**, *12*, 119.
(5) Schmidt-Rohr, K. *Macromolecules* **1996**, *29*, 3975.
(6) Kaji, H.; Schmidt-Rohr, K. *Macromolecules* **2000**, *33*, 5169.
(7) Rizzo, P.; Auriemma, F.; Guerra, G.; Petraccone, V.; Corradini, P. *Macromolecules* **1996**, *29*, 8852.
(8) Hobson, R. J.; Windle, A. H. *Polymer* **1993**, *34*, 3582.
(9) Hobson, R. J.; Windle, A. H. *Macromolecules* **1993**, *26*, 6903.
(10) Robyr, P.; Gan, Z.; Suter, U. W. *Macromolecules* **1998**, *31*, 8918.
(11) Natta, G.; Mazzanti, G.; Corradini, P. *Atti Accad. Naz. Lincei, Cl. Sci. Fis., Mat. Nat., Rend.* **1958**, *25*, 3.
(12) Bohn, C. R.; Schaefgen, J. R.; Statton, W. O. *J. Polym. Sci.* **1961**, *55*, 531.
(13) Lindenmeyer, P. H.; Hosemann, R. *J. Appl. Phys.* **1963**, *34*, 42.
(14) Liu, X. D.; Ruland, W. *Macromolecules* **1993**, *26*, 3030.
(15) See references in ref 6.
(16) Lizak, M.; Gullion, T.; Conradi, M. S. *J. Magn. Reson.* **1991**, *91*, 254.
(17) Utz, M.; Eisenegger, J.; Suter, U. W.; Ernst, R. R. *J. Magn. Reson.* **1997**, *128*, 217.
(18) Schmidt-Rohr, K.; Spiess, H. W. *Multidimensional Solid-State NMR and Polymers*; Academic Press: London, 1994.
(19) Schmidt-Rohr, K. *J. Magn. Reson.* **1998**, *131*, 209.
(20) Harris, D. J.; Bonagamba, T. J.; Schmidt-Rohr, K. *Macromolecules* **1999**, *32*, 6718.
(21) Ernst, R. R.; Bodenhausen, G.; Wokaun, A. *Principles of Nuclear Magnetic Resonance in One and Two Dimensions*; Clarendon Press: Oxford, 1987.
(22) Kaji, H.; Schmidt-Rohr, K. *Macromolecules* **2001**, *34*, 7382.
(23) Lonsdale, K. *International Tables for X-ray Crystallography*; D. Reidel Publishing Co.: Dordrecht, The Netherlands, 1985; Vol. III.
(24) Hennico, G.; Delhalle, J. *J. Chem. Soc., Faraday Trans.* **1990**, *86*, 1025.
(25) Ishii, Y.; Terao, T.; Hayashi, S. *J. Chem. Phys.* **1997**, *107*, 2760.
(26) Yen, Y. S.; Pines, A. *J. Chem. Phys.* **1983**, *78*, 3579.
(27) Baum, J.; Pines, A. *J. Am. Chem. Soc.* **1986**, *108*, 7447.
(28) Shykind, D. N.; Baum, J.; Liu, S.-B.; Pines, A. *J. Magn. Reson.* **1988**, *76*, 149.
(29) Antzutkin, O. N.; Tycko, R. *J. Chem. Phys.* **1999**, *110*, 2749.
(30) Schmidt-Rohr, K.; Kulik, A. S.; Beckham, H. W.; Ohlemacher, A.; Pawelzik, U.; Boeffel, C.; Spiess, H. W. *Macromolecules* **1994**, *27*, 4733.
(31) Bielecki, A.; Kolbert, A. C.; Levitt, M. H. *Chem. Phys. Lett.* **1989**, *155*, 341.
(32) Bielecki, A.; Kolbert, A. C.; de Groot, H. J. M.; Griffin, R. G.; Levitt, M. H. *Adv. Magn. Reson.* **1990**, *14*, 111.

MA010657K